Biophysical Journal
Article

Biophysical Society

Exploring the Formation and the Structure of Synaptobrevin Oligomers in a Model Membrane

Jing Han,[1] Kristyna Pluhackova,[1] and Rainer A. Böckmann[1,*]
[1]Computational Biology, Department of Biology, Friedrich-Alexander Universität Erlangen-Nürnberg, Erlangen, Germany

ABSTRACT SNARE complexes have been shown to act cooperatively to enable the synaptic vesicle fusion in neuronal transmission at millisecond timescale. It has previously been suggested that the oligomerization of SNARE complexes required for cooperative action in fusion is mediated by interactions between transmembrane domains (TMDs). We study the oligomerization of synaptobrevin TMD using ensembles of molecular dynamics (MD) simulations at coarse-grained resolution for both the wild-type (WT) and selected mutants. Trimerization and tetramerization of the sybII WT and mutants displayed distinct kinetics depending both on the rate of dimerization and the availability of alternative binding interfaces. Interestingly, the tetramerization kinetics and propensity for the sybII W89A-W90A mutant was significantly increased as compared with the WT; the tryptophans in WT sybII impose sterical restraints on oligomer packing, thereby maintaining an appropriate plasticity and accessibility of sybII to the binding of its cognate SNARE partners during membrane fusion. Higher-order oligomeric models (ranging from pentamer to octamer), built by incremental addition of peptides to smaller oligomers, revealed substantial stability and high compactness. These larger sybII oligomers may induce membrane deformation, thereby possibly facilitating fast fusion exocytosis.

INTRODUCTION

Intracellular membrane fusion events in eukaryotic cells such as cell growth and neurotransmitter release are mediated by a conserved family of proteins called SNAREs (soluble N-ethylmaleimid-sensitive factor (NSF) attachment protein receptors) consisting of syntaxin and SNAP-25 on the plasma membrane and synaptobrevin-2 (sybII) on synaptic vesicles (1–3). These three proteins zipper up in a directional way from the N-terminus toward the C terminus by their respective SNARE motifs to form a parallel four-helix bundle upon SNARE assembly (4,5). This progressive pairing brings the opposing membranes into proximity and initializes fusion, leading to the formation of a *cis*-SNARE complex accompanying the final membrane merger (6). It is becoming widely accepted that multiple SNARE complexes are essential for efficient fusion (7–10). However, the exact number of SNARE complexes required for membrane fusion as well as the spatial organization of multiple complexes at the fusion site remain unclear.

Different approaches have been used to investigate the number of SNARE complexes involved in the fusion process, leading to different estimates ranging from one to fifteen complexes (8,9,11–15). For example, experiments in cracked PC12 cells revealed that at least three SNARE complexes act cooperatively to mediate fusion (15). Another model proposed that a minimum of four complexes are essential for fusion, based on atomic force microscopy (AFM) measurements of the interaction force between SNARE proteins (16). The SNARE complex isolated from brain tissue was observed to self-assemble into star-shaped bundles containing three to four complexes (17). In another study, a correlation between the fusion efficiency and the SNARE density was established, suggesting that five to eleven SNARE complexes are required for rapid fusion (18). Amperometry and conductance measurements on the native SNARE proteins and their TMD mutants proposed a circular arrangement of five to eight syntaxins forming a proteinaceous fusion pore (13), which is suggested to be complemented by a similar proteinaceous vesicular pore formed by six to eight synaptobrevins, resulting in a direct connection between the plasma and vesicle membranes (19). This variation in the number of SNARE complexes required in fusion reactions may reflect a certain plasticity of SNARE proteins, which would allow assembly of SNARE oligomers in a controllable manner dependent on the vesicle size or local physiological conditions (9,10,20).

The formation of homooligomers of SNARE proteins in the prefusion state has been shown to be mediated by the

Submitted December 30, 2015, and accepted for publication April 6, 2016.
*Correspondence: rainer.boeckmann@fau.de
Editor: Emad Tajkhorshid
http://dx.doi.org/10.1016/j.bpj.2016.04.006

interaction between their transmembrane domains (21–24). These oligomers increase the local concentration of SNARE proteins leading to the formation of multiple SNARE complexes at the fusion site (25,26). Such clusters of SNARE complexes are thought to enable a cooperative action in fusion to provide sufficient energy for rapid fusion (10,12). Alternatively, SNARE TMD oligomers containing at least five SNARE proteins were proposed to form a proteinaceous fusion pore (13,19). Thus exploring the mechanism of SNARE TMD assembly into oligomers and their structure is fundamentally crucial to enhance our understanding of the cooperative action of multiple SNARE complexes in triggering rapid exocytosis fusion and to deduce a possible mechanism of their concerted action.

Crystal structures of SNARE oligomers are extremely difficult to resolve because of their dynamic properties and probably differing oligomer sizes (24,27–29). Computational approaches may assist in exploring the structure and dynamics of both membrane protein assemblies (30–33) and also of soluble oligomers (34). Recently, the dimerization process and different dimer configurations of the synaptobrevin TMD were predicted using a multiscale simulation approach (33). Dimer structures as well as interfacial residues were shown to be in very good agreement with available experimental and computational data (24,33,35). Moreover, alternative binding interfaces were discovered and suggested to be required for the oligomerization of sybII TMD (33).

In this study, we investigated the oligomerization of the sybII transmembrane domain and of selected mutants using ensembles of molecular dynamics (MD) simulations at coarse-grained (CG) resolution. Trimer and tetramer configurations obtained from spontaneous oligomerization simulations set the structural basis for the construction of higher-order oligomers. Compact oligomers were found to be favored over linear aggregates. The preferred configuration with Leu^{99}, Cys^{103}, Leu^{107}, and Ile^{111} at the helix-helix interface is in strong contrast to a recent model based on conductance measurements reporting Leu^{99} and Cys^{103} as well as Val^{101} and Ile^{105} to line the fusion pore (19). The latter two amino acids are suggested here to form part of the outer surface of the sybII TMD bundle, providing a possible interaction site for further sybII peptides as well as for the cognate SNARE partner syntaxin upon *cis*-SNARE complex formation.

MATERIALS AND METHODS

To investigate the underlying mechanisms for spatial organization of SNARE oligomers, self-assembly sybII TM trimerization and tetramerization were studied at CG resolution from self-assembly simulations using large ensembles of simulations. Larger oligomers comprising five to eight TMDs were predicted based on self-assembled tetramer configurations following a specific "propagation" pattern detailed below.

TMD sequences of sybII and selected mutants with different effects on membrane fusion were used in the study of sybII oligomerization, i.e., the wild-type (WT), a WWAA mutant (exhibiting altered priming but possessing the same fusion efficiency as the WT (36)), and a PolyL mutant (showing reduced fusion activity (37)), see Table 1. Spontaneous trimerization was studied based on large ensembles (~500) of CG-MD simulations (5 μs each) for the sybII WT, WWAA, and PolyL mutants. Tetramerization analysis was restricted to the WT and the WWAA mutant, using again large ensembles (~500 of 5 μs each).

CG systems for trimerization and tetramerization studies were prepared according to the procedure described in our previous work (33). The systems for the trimerization study contained $\approx$160 lipids, $\approx$1100 water beads, and three copies of TM helices (WT, WWAA, or PolyL). Systems for tetramerization consisted accordingly of $\approx$220 lipids, $\approx$1420 water beads, and 4 copies of helical peptides (WT or WWAA). A summary of the simulation systems studied is given in Table 2. All CG simulations were performed using the GROMACS software package, version 4.5.2 (38), together with the Martini force field (39,40) and the standard Martini water model. An NpT ensemble was employed to carry out the production simulations of length 5 μs each. A time step of 20 fs was used and trajectories were recorded every 500 ps. The temperature was weakly coupled using the Bussi velocity rescale algorithm (41) at 310 K, with a coupling constant of 1.0 ps. The system pressure was coupled semi-isotropically using the Berendsen algorithm (42) at 1 bar, with a coupling time of 3.0 ps and a compressibility of 3.0×10^{-4} bar^{-1}. Electrostatic interactions were smoothly shifted to zero between 0 and 1.2 nm with a relative dielectric constant of 15, and the Lennard-Jones interactions were shifted to zero between 0.9 and 1.2 nm. The nonbonded neighbor lists were updated every 10 steps. The total simulation times for trimer and tetramer formation were $\approx$2.5 ms in total for each setup, which corresponds to effective time of $\approx$10 ms (scaled by a factor of 4 (39)).

Due to the significant increase in simulation time required to form higher-order oligomers using self-assembly simulations, larger oligomers were built manually using the tetramer configuration as a starting point: to find the energetically most favorable model, a library of dimer structures with lowest energy was used as a repository (taken from (33)). To build up a pentamer model, one helix from a dimer structure was fitted to a helix of a tetramer configuration with an available free binding interface (i.e., a peripheric helix). The resulting oligomer models were then screened to exclude conformations with van der Waals overlaps. Higher-order oligomers were built in a similar way, on the basis of oligomers that are smaller by one molecule. In this way, oligomers containing five to eight helices were built up in a stepwise manner by adding one peptide via least-square fitting of a dimer structure to the peripheric peptide of an oligomer with one helix less. The obtained oligomeric structures of sybII with varying size were subsequently minimized in vacuum, and solvated by Martini POPC lipids and water molecules using the *insane* scheme (43,44). The resulting systems were energy-minimized, equilibrated, and subjected to production MD simulations of 5 μs each at CG resolution.

Backmapping of equilibrated compact trimer and tetramer structures at CG resolution to atomistic resolution (45) enabled subsequent structural analysis using atomistic MD simulations. The obtained atomistic structures including protein, membrane, and solvent were energy minimized for 500 steps and equilibrated for 2 ns restraining the protein backbone atoms. The production atomistic simulations were carried out for 200 ns each using the GROMACS package, version 4.5.2 (38), with the CHARMM36 force field (46,47) and the CHARMM variant of the TIP3P water model (48). The long-range electrostatic interactions were treated using the particle

TABLE 1 Amino-Acids Sequences of SybII TMD WT, WWAA, and PolyL Mutants

Peptides	Sequences
WT	85–KRKYWWKNLKMMIILGVICAIILIIIIVYFST–116
WWAA	85–KRKYAAKNLKMMIILGVICAIILIIIIVYFST–116
PolyL	85–KRKYWWKNLKMMLLLLLLLLLLLLLLLYFST–116

Mutation sites are underlined.

TABLE 2 Summary of Performed Simulations for SybII TMD Oligomerization

Simulation	Peptide Conformation	Duration (μs)
CG Simulations		
WT-trimer	3 monomers	518 × 5
WWAA-trimer	3 monomers	487 × 5
PolyL-trimer	3 monomers	520 × 5
WT-tetramer	4 monomers	517 × 5
WWAA-tetramer	4 monomers	492 × 5
WT-pentamer	1 pentamer	5
WT-hexamer	1 hexamer	5
WT-heptamer	1 heptamer	5
WT-octamer	1 octamer	5
AA Simulations		
WT-trimer	1 compact trimer	0.3
WT-trimer	1 linear trimer	0.3
WWAA-trimer	1 compact trimer	0.2
WWAA-trimer	1 linear trimer	0.2
PolyL-trimer	1 compact trimer	0.2
PolyL-trimer	1 linear trimer	0.2
WT-tetramer	1 tetramer	0.2
WWAA-tetramer	1 tetramer	0.2

mesh Ewald method (49) beyond 1.2 nm. The van der Waals interactions were switched to zero between 0.8 and 1.2 nm. The Parrinello-Rahman barostat (50) was used for semi-isotropic pressure coupling at 1 bar with a time constant of 1.0 ps, whereas Nosé-Hoover thermostat (51,52) was used for the temperature coupling at 310 K with a time constant of 1 ps. The time step for the simulation was set to 2 fs and the neighbor-list was updated every 10 steps. The LINCS algorithm (53) was used to constrain covalent bonds to hydrogen atoms. The analyses were performed using GROMACS utilities and in-house codes, whereas visualization was conducted in PyMOL (54) and VMD (55).

RESULTS AND DISCUSSION

TMD trimerization pathway

All trimerization simulations were started from three isolated helices arranged in a parallel fashion and separated by ≈4.5 nm between each pair, together with a random in-plane rotation for each helix, aiming to avoid any biased interactions between helices before simulation. The formation of trimers was evaluated by monitoring the evolution of center of mass distances between pairwise helices. The assembly of a trimeric structure was in almost all simulations initiated by the formation of a dimer structure, which resembles the association behavior described previously for sybII TMD dimerization (33). Subsequently, the isolated helix engages with the dimer structure via interactions between the C termini, resulting in the formation of a trimer with three helices in a linear arrangement (see Fig. 1 for a typical trimer assembly simulation). This configuration may transit to a compact trimer or keep its original shape on the microsecond timescale (5 μs simulation time). This suggests that apart from its crucial role in sybII dimerization (33), the C terminus of sybII TMD also assists in the formation of higher-order oligomers by establishing the initial contact between helices, explaining the functional significance of the C terminus of sybII TMD in membrane fusion, as described in earlier experimental studies (56–58).

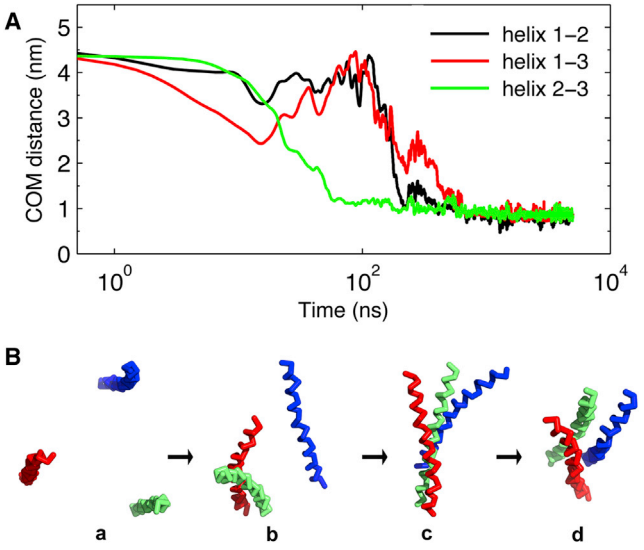

FIGURE 1 Time evolution of center of mass distances between pairwise helices for a sample trimerization simulation (*A*), and representative conformations at specific positions during the formation of the trimer (*B*): (*a*) three isolated monomers, (*b*) dimer formation, (*c*) formation of a linear trimer, and (*d*) rearrangement to a compact trimer. The three helices (1–3) are colored in blue, red, and green, respectively. To see this figure in color, go online.

A similar trimerization pathway was also observed for WWAA and PolyL mutants, following the same propagational characteristics. However, the trimerization kinetics as well as the preferred geometry differ remarkably, especially for the PolyL mutant, suggesting an important role of the TMD primary sequence in oligomerization of synaptobrevin.

Trimerization kinetics depends on helix association profile

To characterize the oligomerization kinetics, the concentration of trimers over the whole ensembles (≈500 simulations for each system) was evaluated and is shown in Fig. 2 *B*. In total, 99.2% of all WT and 97.6% of WWAA simulations trimerized within the simulation time, whereas PolyL formed trimers only in 70.9% of the simulations. The buried accessible surface area (BASA), defined as the difference between the solvent accessible surface area (SASA) of a dimer and the SASAs of individual monomers, was used to assess the self-association of TMDs in the membrane, which has been shown to be a suitable indicator to monitor the evolvement of protein contacts (59). The total BASA for each configuration was calculated and compared with the maximal values reported previously for stable dimer structures (33). This maximum was used as a cutoff (lower bound) to define the formation of trimer structures with an additional peptide-peptide contact. The relative distribution

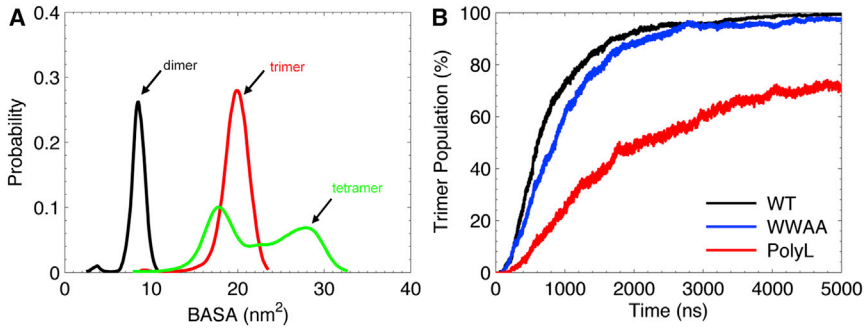

FIGURE 2 (*A*) Distributions of the total buried accessible surface area (BASA) for sybII WT oligomers (trimer and tetramer) from simulation ensembles after 5 μs (averaged over final 100 ns of all simulations). The BASA distribution for the dimerization ensemble is provided for reference and was calculated from a previous simulation study (33). (*B*) Populations of trimer structures for the WT and the mutants as a function of simulation time over the whole ensembles are shown. To see this figure in color, go online.

of BASA values was evaluated for the final 100 ns of all 5 μs long simulations of the sybII oligomer (trimer and tetramer) ensembles (Fig. 2 *A*).

Fig. 2 *B* shows the populations of trimer structures composed of both linear and compact aggregates over all simulations for the WT and the mutants (WWAA, PolyL). Clearly, the WWAA mutant shows similar trimerization kinetics as compared with the WT. For both WT and WWAA, after 5 μs trimers were formed in nearly all simulations. Both sequences were shown to adopt similar dimerization kinetics as well as multiple dimerization interfaces (33). In contrast, a remarkably decreased trimerization kinetics (Fig. 2 *B*) was observed for the fusion inactive mutant (PolyL). This discrepancy in sybII trimerization between the WT and the PolyL mutant demonstrates that the available binding interfaces as well as the TMD-TMD association profiles explored from dimerization (33) determine the kinetics and organization in the oligomer assembly.

The difference in trimerization kinetics is as well reflected by the average time for trimer formation (T_f). As compared with the sybII WT with a T_f of $\approx$550 ns, a significantly increased $T_f \approx 1140$ ns was determined for the PolyL mutant, whereas the WT and the WWAA mutant ($T_f \approx 690$ ns) had comparable formation times.

Tetramer formation via distinct pathways

In the above sections, we have shown that the formation of the sybII trimer proceeds via propagation in a "monomer-dimer-trimer" order. As expected, most tetramers of sybII TMD were formed on the basis of assembled trimer structures, followed by C-terminal attachment of a fourth TM helix and rearrangement of the metastable four-helical bundle into an energetically more favorable compact tetramer configuration (Fig. 3 *A*). Alternatively, the formation of tetramers in linear geometry processes via aggregation of two preassembled dimers.

Although a similar tetramerization pathway was observed for the WWAA mutant, a remarkably enhanced association kinetics is seen as compared with the WT (Fig. 3 *B*). In 69% of the simulations, tetramers were formed for WWAA within 5 μs, whereas only $\approx$33% of the whole ensemble led to tetramer configurations for the WT. Accordingly, the average time required for tetramer formation was $\approx$2700 ns for the WT, significantly longer than for the WWAA mutant ($\approx$1760 ns). The critical step in the formation of tetramers is the evolution from the trimer configuration to the tetramer configuration, which requires an optimal packing to accommodate multiple helices in an energetically feasible way. Our results suggest that the optimal packing in organization of sybII oligomers ($N \geq 4$) is largely influenced by the bulky tryptophan residues ($W^{89}W^{90}$) in the interfacial area, which impose a steric hindrance on the packing of TM helices. This inhibition in the packing kinetics is clearly reflected in the decreased transition rate for the WT from the trimer to tetramer configuration as compared with the respective rate for the WWAA mutant (Fig. 3 *B*, *magenta lines*). Interestingly, the larger population for the "dimer + dimer" configurations as compared with the "trimer + monomer" configurations (Fig. 3) implies a higher propensity for the "propagational" mechanism in tetramer formation; i.e., a tetramer structure is more probably formed by the continuous growth in oligomer size than by aggregation of smaller multimers.

Similar to the trimers, the sybII WT tetramers also assumed two distinct configurations, i.e., linear and compact configurations. As compared with the WT, the WWAA mutant adopted a significantly increased population of compact tetramer configurations. This difference is partly explained by the enhanced interconversion rate from the linear configuration to the energetically more stable compact tetramer configuration for the WWAA mutant (0.31 for linear-compact vs. 0.19 for compact-linear interconversions for WWAA, see Fig. 3, *B* and *C*). The high bidirectional interconversion rates for the WT (Fig. 3 *C*) demonstrate that apart from decreasing the tetramerization kinetics, the bulky tryptophan residues ($W^{89}W^{90}$) also enhance the conformational flexibility of WT tetramers by facilitating a fast interconversion between linear and compact tetramers.

It is interesting to note that compact bundles tend to adopt a uniform interhelical crossing angle for pairwise helices in either right-handed (RH) or left-handed (LH) geometry. In contrast, for the linear tetramer, a progressive connection was established between two assembled RH dimers by a

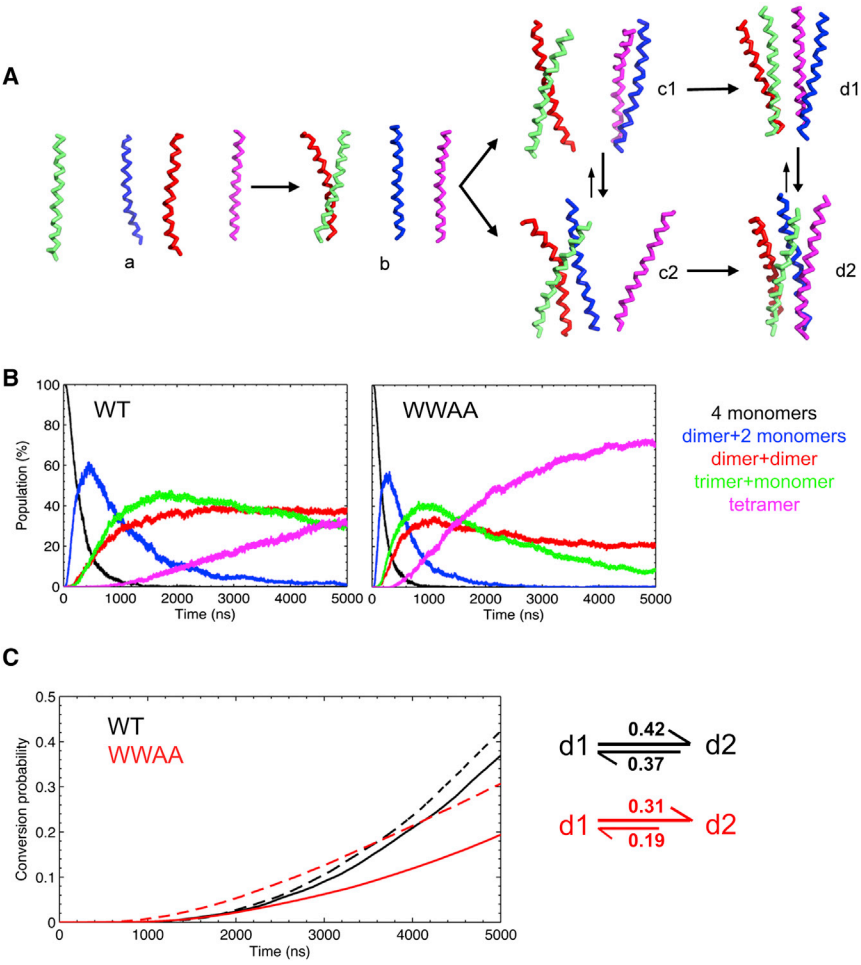

FIGURE 3 Tetramerization of sybII TMD. (*A*) Evolvement of different conformations in the tetramerization process: monomer (*a*), dimer (*b*), dimer + dimer (*c1*)/trimer + monomer (*c2*), and tetramer (linear (*d1*) and compact (*d2*)). These configurations are involved in two tetramerization pathways with possible interconversions between individual states. (*B*) Relative populations of distinct configurations in the process of self-assembly of tetramers for both WT and WWAA. (*C*) Cumulative interconversion probabilities between compact (*d2*) and linear tetramers (d1). Conversions from *d1* to *d2* and the reversed reaction (*d2* to *d1*) are shown (*dashed versus solid lines*), with the total conversion probability after 5 μs indicated. For each simulation, linear and compact tetramer configurations were determined based on BASA and the number of interacting helices. A transition event between linear and compact tetramers was counted if the new configuration was stable for at least 10 ns. The cumulative interconversion probability was defined by the cumulative linear tetramer (compact tetramer) population divided by the total number of conversion events from a linear to a compact tetramer configuration (compact to linear tetramer). To see this figure in color, go online.

LH geometry to obtain an optimal packing. This structural feature renders the linear tetramer extendable to larger clusters by recruitment of new dimers.

Packing properties of sybII trimer/tetramer structures

The rapid spontaneous trimer formation confirms our hypothesis of the importance of multiple binding interfaces for oligomerization (33). However, it remains to be confirmed whether the same binding interfaces are involved in sybII trimerization and dimerization. The relative orientation between two neighboring helices in trimer structures with both compact and linear geometries can be described by the relative binding positions β and χ (defined in Fig. 4 *A*).

The most populated dimer binding interface (33), I-c1, contributed strongly to the self-assembly of sybII trimers (Fig. 4, *B* and *C*). In addition, the alternative binding interfaces for a linear trimer resembles well those reported for dimers (Fig. 4 *C*). In contrast, a shift in binding position was observed for these alternative interaction interfaces in the case of compact trimers (B), reflecting a substantial plasticity by maintaining an optimal packing of the helices. In addition, the binding interfaces (data not shown) for adjacent helices in tetramers was similar to dimerization and trimerization interfaces.

Similar binding patterns were also observed for the WWAA and PolyL mutants (data not shown). The ratio between compact and linear trimers for the WT (139:100) is remarkably larger than that for WWAA (40:100), reflecting a strong preference of WWAA trimers for a linear geometry. Given the similar propensities of WT and WWAA for the main and the alternative binding interfaces (33), it can be concluded that for WWAA the stability of the linear trimer is increased as compared with that of the WT, resulting in a decreased probability for the transition to compact aggregates.

Apart from the binding interfaces contributing to the assembly of sybII oligomers, the crossing angle between adjacent helices exhibited a similar characteristics as for the dimers, as indicated in Fig. 5. The packing between two neighboring helices for sybII oligomers (N = 3,4) showed a distribution similar to the one for dimers. The conformational plasticity in the sybII oligomers is reflected in the broadened distributions. It is interesting to note that

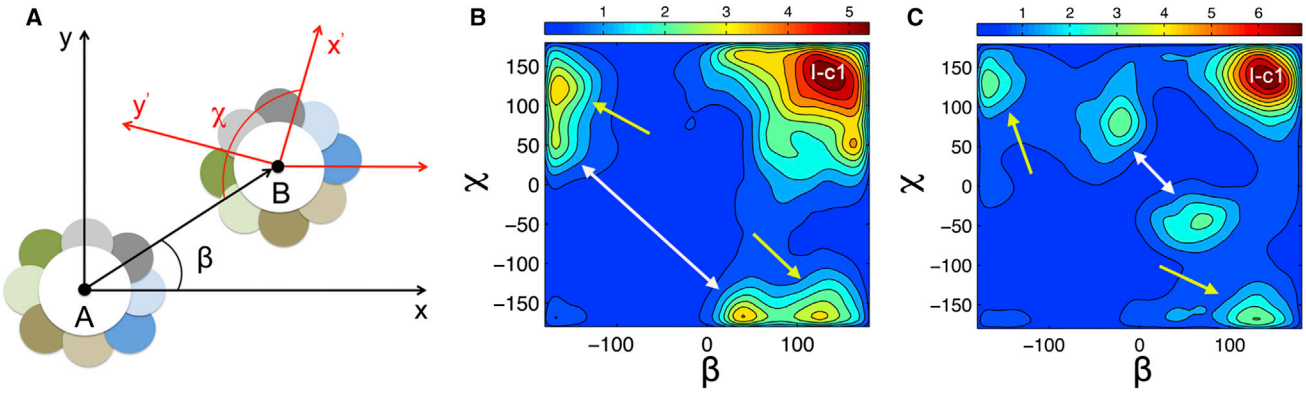

FIGURE 4 Binding orientation (*A*) of interacting pairs of helices for trimer structures in compact (*B*) and linear shape (*C*), characterized by the probability distribution (artificial units) of relative binding positions (β) and (χ) for the WT. The *x* and *y* axes in (*A*) were arbitrarily chosen. The dominant binding interface (I-c1) as well as alternative binding interfaces are marked by white and yellow arrows. The alternative binding interfaces show a moderate shift for the packing in compact trimers, whereas the same interaction surfaces were found for linear trimers as compared to those previously reported for a dimer ensemble (33). To see this figure in color, go online.

the relative probability for the LH geometry increased with a growing oligomer size.

Residues $L^{99}/C^{103}/L^{107}/I^{111}$ contribute to helix packing in sybII oligomers

Interestingly, the residues (L^{99}, C^{103}, L^{107}, I^{111}) critical for sybII TMD dimerization and reported to constitute the main binding interface (22–24,33) were found to orient toward the binding interfaces between neighboring helices in sybII oligomers, as shown in Fig. 6 for trimer and tetramer configurations obtained after 200 ns atomistic simulations of self-assembled compact trimer and tetramer structures from CG simulations. These residues also contribute most significantly to the interactions within sybII oligomers as seen from the contact maps between pairwise residues in Fig. 7. Interestingly, these residues have recently been proposed to constitute a proteinaceous fusion pore with the side chains pointing into the pore lumen, in combination with two other residues (V^{101}, I^{105}), which reside on the opposite side of the helical face (19). Mutation of these residues to bulky tryptophans resulted in a significantly reduced fusion pore flux (19). From the structural perspective gained here, it appears unlikely that these residues orient toward the luminal space of the fusion pore, but rather influence the assembly of sybII oligomers. It is apparent that the two pairs of residues (L^{99}/C^{103}, V^{101}/I^{105}) at opposite sites of the helix represent two alternative binding surfaces (33) and provide free binding sites to recruit isolated sybII molecules to form larger oligomers. Already for sybII tetramers, the residues V^{101}/I^{105} were found to contribute to the total interaction energy (see Fig. 7, *right panel*, for the interaction map) by involving the fourth protomer to the compact trimer structure (see Fig. 6). Replacement of these interfacial residues by tryptophans thus likely inhibits the oligomerization of sybII TMD.

In addition to the above residues, the trimer and tetramer configurations suggest an important role of G^{100} in packing because of its orientation toward the helical interface (see Fig. 9) where it interacts with C^{103} (see Fig. 7). An additional important function of G^{100} is to increase the flexibility of the TMD by introducing a helix kink (60,61) between the upper (residues 90–98) and the lower (residues 102–115) part of the TMD. The ability of the Martini force field to reproduce the peptide kink observed in atomistic simulations (60,61) and the influence of oligomerization on the

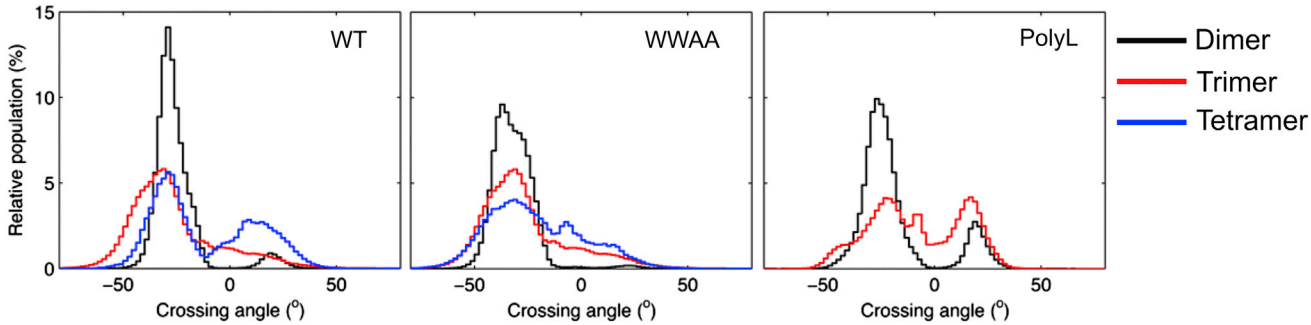

FIGURE 5 Distribution of interhelical crossing angles for adjacent helices of sybII oligomers ($N = 3,4$) for WT, WWAA, and PolyL. The relative distribution for associated helices from a dimerization study is provided for comparison (*black*) (33). To see this figure in color, go online.

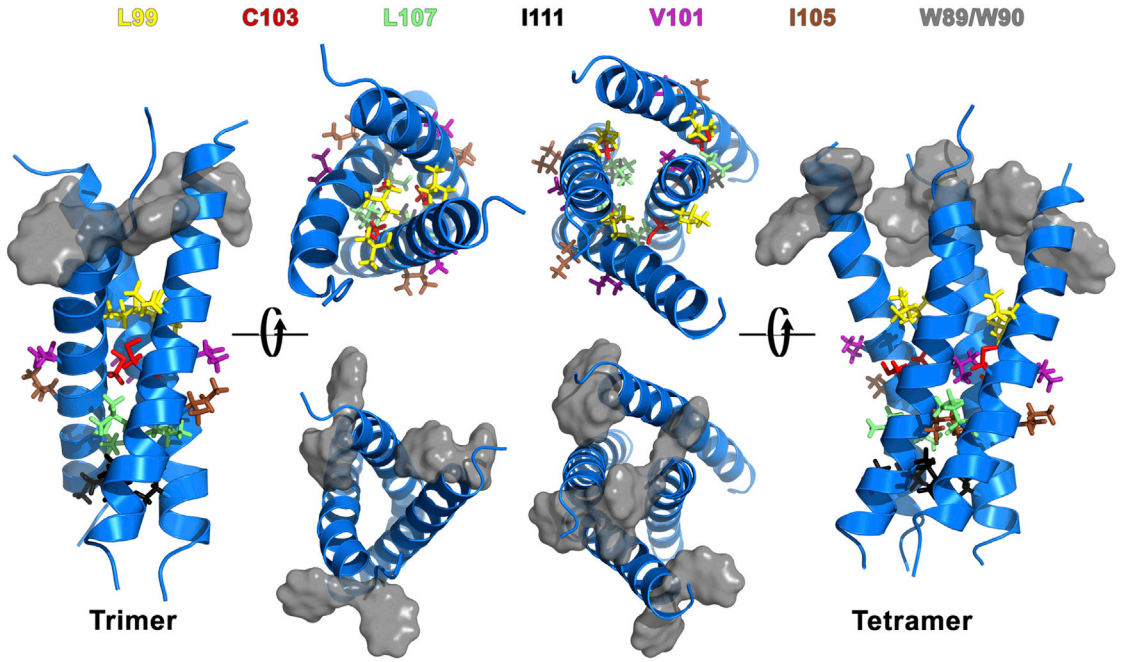

FIGURE 6 Structures of sybII compact trimer and tetramer configurations. The snapshots show structures after 200 ns atomistic simulation after back-mapping of CG structures. Critical residues for dimerization, $L^{99}/C^{103}/L^{107}/I^{111}$, as well as V^{101}/I^{105} that were suggested before to point toward the pore lumen of sybII fusion pores (19), are shown in stick representation. V^{101} and I^{105} are pointing outward. Tryptophane residues are shown as gray surfaces. To see this figure in color, go online.

kink angle were analyzed by comparison of the kink angles observed in simulations of monomeric, trimeric, and tetrameric sybII configurations both at atomistic and CG level (see Fig. 8).

The peptides in CG representation are only slighly less kinked (by ~2°) as compared with atomistic simulations, independent of the oligomerization state of the peptide. In trimer configuration, the kink was slightly increased and the distribution broadened as compared with both sybII monomer and tetramer configurations suggesting an increased adaptation of the peptides in this configuration.

From tetramers to higher-order oligomers

Although one SNARE complex was shown to be sufficient to induce membrane fusion in an in vitro liposome fusion

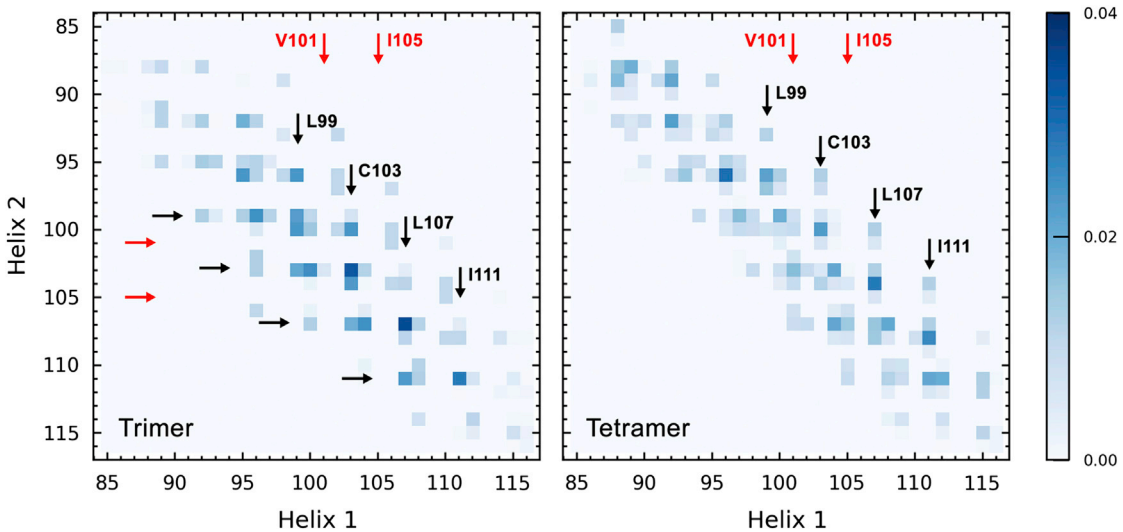

FIGURE 7 Contact maps displaying pairwise interaction frequencies for residues involved in the formation of trimer (*left*) and tetramer configurations (*right*). To see this figure in color, go online.

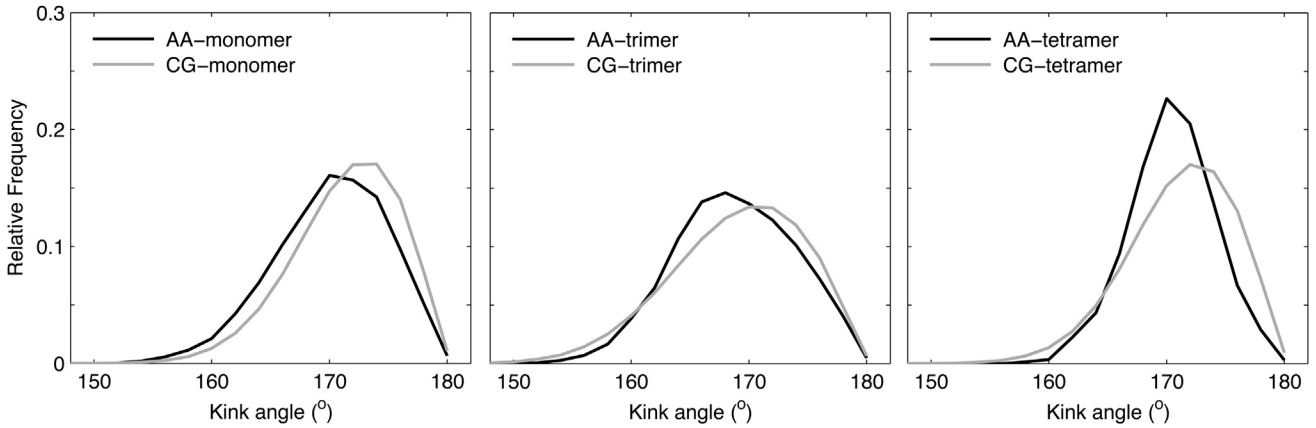

FIGURE 8 Distribution of kink angles at G^{100} for monomeric, trimeric, and tetrameric WT sybII as observed in atomistic (*black line*) and CG (*gray line*) simulations.

experiment (11), a wealth of studies revealed that multiple SNARE complexes are required for fast in vivo exocytosis or reconstituted liposome fusion (8,10,56,62). The number of complexes varied with the experimental or physiological conditions (20). A theoretical model based on a single vesicle fusion event revealed that eight SNARE complexes are optimal to accomplish fusion with rates compatible with that for in vivo neurotransmission (63). It has previously been noticed that syntaxin is distributed in clusters of different sizes, and small clusters were found to unite to form large clusters that are suggested to serve as a reservoir and define the sites for fusion reactions (64). However, the functional organization of multiple SNARE complexes remains poorly understood.

Using self-assembly for sybII trimerization and tetramerization on ensembles of CG simulations, we have shown that most sybII oligomers assembled following a specific pattern by which pairwise helix interactions well resemble those explored in sybII dimerization (33). An overall similarity between the helix binding interfaces as well as packing geometry was seen between sybII oligomers (trimers or tetramers) and dimers (see previous section), albeit a slight structural adaption exists with increasing complexity of the systems.

Based on the "propagational" growing pattern observed upon trimer and tetramer formation, oligomeric models were built by combining dimer structures with alternative binding interfaces and assembled tetramers. As a proof of principle, we compared representative self-assembled trimer and tetramer structures with those from a combination of multiple dimers with alternative binding interfaces, as shown in Fig. 9. Trimer structures obtained from spontaneous association and from manual assembly showed a good agreement with an RMSD value of 0.26 nm. A slightly larger deviation (RMSD = 0.51 nm) was observed between the self-assembled tetramer and that formed by combination of three different dimers. This implies an enhanced flexibility with increasing size of sybII oligomers in self-assembly simulations, during which a slight structural rearrangement may occur. However, the orientation of individual peptides in the oligomer is equal. The observed similarity in sybII packing between oligomers and dimers supports the assumption that the helix-helix association profiles explored in dimerization may serve as a reliable basis to predict higher-order oligomeric states at a drastically reduced computational cost.

The conformational stability of the sybII oligomeric structures (pentamer, hexamer, heptamer, and octamer)

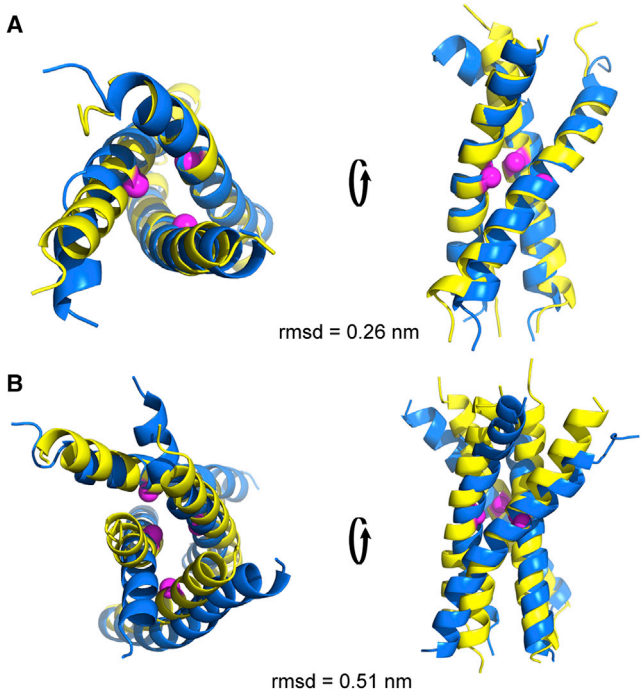

FIGURE 9 Alignment of sybII trimer (*A*) and tetramer (*B*) structures from self-assembly CG-MD simulations (*yellow*) and from simulations of manual combinations of multiple dimers with different binding interfaces (*blue*) (33). The residue G^{100} is shown in sphere representation (*magenta*). To see this figure in color, go online.

was assessed by calculating the root mean-square deviation (RMSD) of the backbone beads from 5μs CG-MD simulations. All the oligomeric structures showed a remarkable stability with RMSD values fluctuating between 2 and 4 Å, with the exception of the octamer with RMSD values ranging between 2 and 6 Å (Fig. 10 *A*). Interestingly, the hexamer configuration with a symmetric geometry displayed an extraordinary stability (RMSD of $\approx$2 Å). Inspection of the trajectories showed that the formation of higher-order oligomers involved subtle structural rearrangements to accommodate the added monomer. The residues L^{99}, C^{103}, L^{107}, and I^{111} point toward the interface between adjacent helices for all oligomers investigated (see Fig. 10 *B*). The dimerization study on sybII TMD suggested a symmetric (face to face, I-c1) or an asymmetric binding mode (face to back, denoted as III before) between the two TMD helices (33). The specific "face to back" pattern appears to be functionally relevant for the organization of sybII TMD oligomers, possibly enabling a plasticity in the assembly of sybII aggregates (20).

Possible influence of juxtamembrane domain (JMD) on the formation of higher-order oligomers

A possible impact of the extracellular domain of sybII on the spatial organization of sybII oligomers was investigated using a short version of full-length sybII (residues 74–116). This construct contains, apart from the TMD, also a short juxtamembrane domain (JMD). Results of an atomistic MD simulation study on the microsecond timescale of sybII monomers containing linker and JMD (61) were used to investigate the plausibility of the above described oligomer configurations for the truncated sybII. In detail, 500 atomistic structures sampled from the final 500 ns of a microsecond simulation (61) were fitted on their TMD and overlaid on the TMD of each protomer in the oligomers described above.

As indicated in Fig. 11, the JMD shows only small overlaps within the sybII oligomers containing three, four, and six TM helices. In contrast, moderate overlaps in the JMD sampling region emerged for sybII heptamer and octamer configurations (N = 7,8). This implies a potential impact on sybII oligomerization: large oligomers restrict the accessible conformational space for the JMD, thus decreasing the propensity for their formation. The presence of the cytosolic domain was suggested before to prevent the formation of sybII oligomers (24). Similarly as described here for sybII, it has previously been proposed that a balance between the steric hindrance caused by the syntaxin cytosolic domain and the lateral association of TMD determines the size and dynamics of syntaxin oligomeric structures (65). It remains to be studied how the cytosolic domains and transmembrane domains cooperate in sybII oligomerization, considering the high density of sybII in the synaptic vesicle membrane (66).

CONCLUSIONS

The cooperation of SNARE complexes is known to be indispensable in driving fast neuronal exocytosis, which requires the assembly of SNARE complexes into oligomers before fusion. The oligomerization of the SNARE complex is thought to be mediated by lateral association of TMDs. In this study, we investigated the oligomerization of the sybII TMD combining high-throughput ensemble simulations at CG resolution. Obtained compact trimer and tetramer structures were stable in subsequent atomistic MD simulations with RMSD values below 4 Å (data not shown, see Fig. 6).

In self-assembly simulations, the trimerization of sybII WT TMD and of its mutants, WWAA and PolyL, was

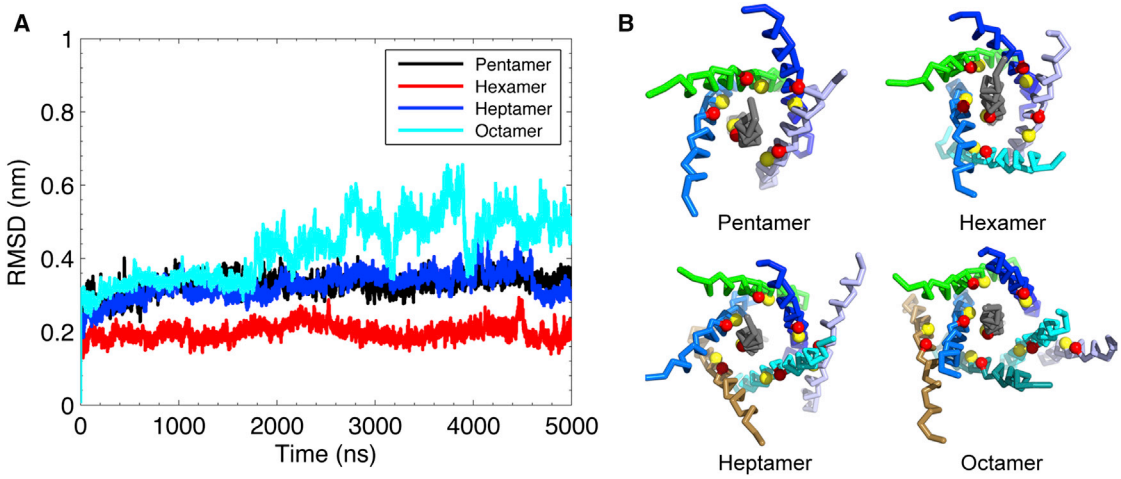

FIGURE 10 (*A*) Structural stability of sybII oligomeric structures assessed by RMSD of backbone beads relative to the starting structure. (*B*) Final snapshots for sybII oligomers after 5 μs CG-MD simulations are provided. Individual helices are colored differently. The two crucial interfacial residues L^{99} (*red spheres*) and C^{103} (*yellow spheres*) are shown to highlight the position of the main interaction interface. To see this figure in color, go online.

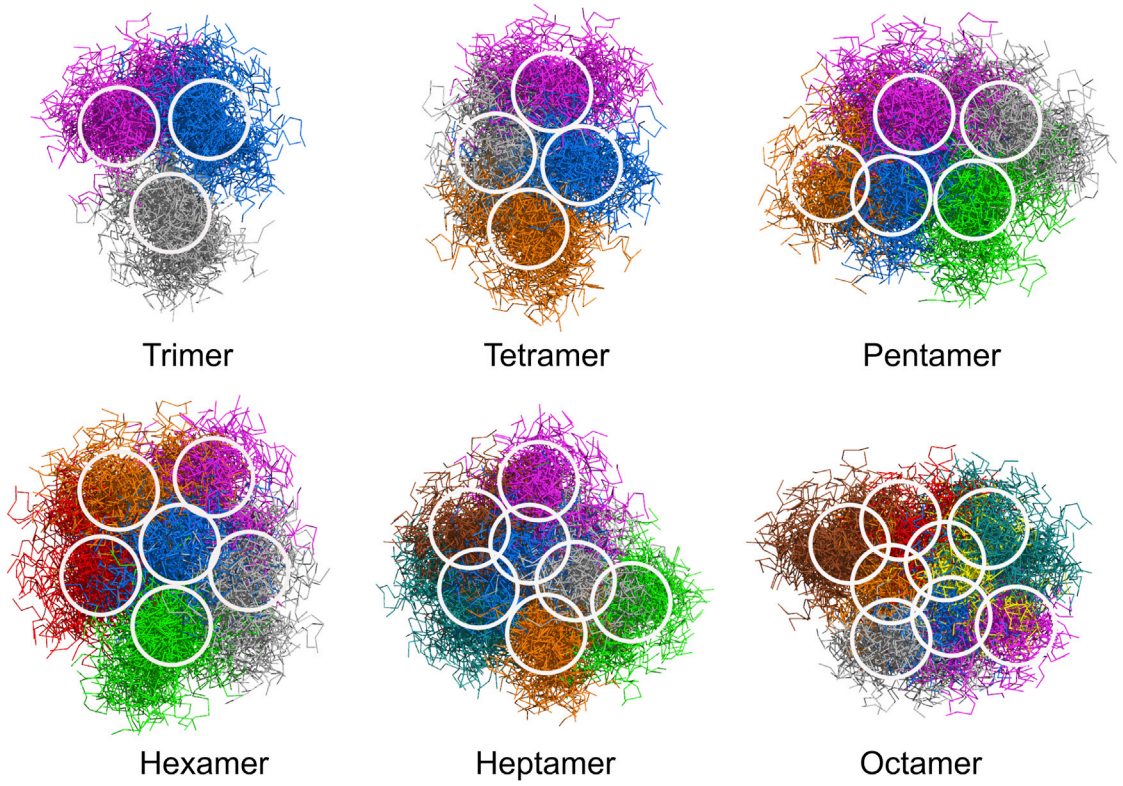

FIGURE 11 Configurations of atomistic sybII constructs (residues 74–116) including the membrane proximal region overlaid and fitted to the TMD of the oligomers described in this study. The regions with largest JMD density are highlighted by circles. To see this figure in color, go online.

initiated at the C termini, followed by formation of a stable crossed dimer. The subsequent engagement of the third isolated helix to the dimer led to the formation of trimer configurations with either linear or compact geometries. The WT and mutants showed a similar trimerization pathway but different kinetics, in particular the PolyL mutant had a remarkably decreased trimerization speed. This difference could be attributed to the lower dimerization kinetics and the lack of alternative binding interfaces for the PolyL mutant, confirming a previous suggestion based on sybII dimerization (33). As expected, a similar trimerization profile was found for the WT and the WWAA mutant explained by their comparable dimerization characteristics.

Similar to the trimerization, the spontaneous formation of a tetramer structure followed a specific dimer → trimer → tetramer pathway. Alternatively, the binding of two assembled dimers could lead to the formation of a tetramer, albeit at a decreased probability. The WT showed a significantly decreased kinetics as compared with the WWAA mutant, suggesting an inhibitory role of the bulky tryptophan residues at the membrane interfacial region in the formation of sybII oligomers ($N \geq 4$). The presence of $Trp^{89}Trp^{90}$ not only decreased the propensity for higher-order oligomers but as well increased the flexibility of the helical bundle as reflected by the increased interconversion probability between linear and compact tetramers. This conformational flexibility is suggested to be important in maintaining the accessibility of sybII molecules to its cognate partner upon SNARE complex formation.

The trimer and tetramer structures obtained from self-assembly simulations showed a striking consistency with the models built by manual combination of dimer structures (Fig. 9), thus offering a computationally less demanding way to model sybII higher-order oligomers ($N \geq 5$). Accordingly manually constructed sybII oligomers ($N = 5,6,7$) showed a high structural stability with RMSD values below 4 Å (exception: octamer RMSD ≈6 Å). The symmetric hexamer bundle exhibited the largest stability with a RMSD of ≈2 Å. Residues Leu^{99}, Cys^{103}, Leu^{107}, and Ile^{111} reported to be important in sybII helix association, were found to be oriented toward the interface with neighboring sybII TMDs. This demonstrates that these residues are also essential to maintain the organization of sybII oligomers. Interestingly, the residues Val^{101} and Ile^{105}, which were proposed before to point toward the central fusion pore formed by sybII TMD (19), are predicted to be located at the outside of the sybII TMD bundle. They are thus freely accessible, e.g., to other free sybII molecules or, alternatively, these residues may provide an interaction site for the cognate SNARE partner, syntaxin, upon *cis*-SNARE complex formation.

Based on the compact geometry of sybII oligomers, we conclude that their main function in the prefusion state is to locally increase the sybII concentration at the fusion site.

AUTHOR CONTRIBUTIONS

R.A.B. designed the research; J.H. performed the simulations; J.H. and K.P. did the analysis; and J.H., K.P., and R.A.B. wrote the manuscript.

ACKNOWLEDGMENT

We thank Tsjerk Wassenaar for insightful discussions.

This work was supported by the German Science Foundation (DFG) within the project BO2963/2-1 and the Research Training Group 1962—Dynamic Interactions at Biological Membranes (J.H., K.P., and R.A.B.). This work was also supported by a scholarship from the China Scholarship Council CSC (J.H.). Computer time was provided by the Computing Center of the University Erlangen-Nürnberg (RRZE).

REFERENCES

1. Jahn, R., and R. H. Scheller. 2006. SNAREs—engines for membrane fusion. *Nat. Rev. Mol. Cell Biol.* 7:631–643.
2. Rizo, J., and C. Rosenmund. 2008. Synaptic vesicle fusion. *Nat. Struct. Mol. Biol.* 15:665–674.
3. Sutton, R. B., D. Fasshauer, …, A. T. Brunger. 1998. Crystal structure of a SNARE complex involved in synaptic exocytosis at 2.4 Å resolution. *Nature.* 395:347–353.
4. Gao, Y., S. Zorman, …, Y. Zhang. 2012. Single reconstituted neuronal SNARE complexes zipper in three distinct stages. *Science.* 337:1340–1343.
5. Hernandez, J. M., A. Stein, …, R. Jahn. 2012. Membrane fusion intermediates via directional and full assembly of the SNARE complex. *Science.* 336:1581–1584.
6. Stein, A., G. Weber, …, R. Jahn. 2009. Helical extension of the neuronal SNARE complex into the membrane. *Nature.* 460:525–528.
7. Tokumaru, H., K. Umayahara, …, T. Abe. 2001. SNARE complex oligomerization by synaphin/complexin is essential for synaptic vesicle exocytosis. *Cell.* 104:421–432.
8. Mohrmann, R., H. de Wit, …, J. B. Sørensen. 2010. Fast vesicle fusion in living cells requires at least three SNARE complexes. *Science.* 330:502–505.
9. Cho, W. J., A. Jeremic, and B. P. Jena. 2005. Size of supramolecular SNARE complex: membrane-directed self-assembly. *J. Am. Chem. Soc.* 127:10156–10157.
10. Montecucco, C., G. Schiavo, and S. Pantano. 2005. SNARE complexes and neuroexocytosis: how many, how close? *Trends Biochem. Sci.* 30:367–372.
11. van den Bogaart, G., M. G. Holt, …, R. Jahn. 2010. One SNARE complex is sufficient for membrane fusion. *Nat. Struct. Mol. Biol.* 17:358–364.
12. Sinha, R., S. Ahmed, …, J. Klingauf. 2011. Two synaptobrevin molecules are sufficient for vesicle fusion in central nervous system synapses. *Proc. Natl. Acad. Sci. USA.* 108:14318–14323.
13. Han, X., C.-T. Wang, …, M. B. Jackson. 2004. Transmembrane segments of syntaxin line the fusion pore of Ca2+-triggered exocytosis. *Science.* 304:289–292.
14. Keller, J. E., F. Cai, and E. A. Neale. 2004. Uptake of botulinum neurotoxin into cultured neurons. *Biochemistry.* 43:526–532.
15. Hua, Y., and R. H. Scheller. 2001. Three SNARE complexes cooperate to mediate membrane fusion. *Proc. Natl. Acad. Sci. USA.* 98:8065–8070.
16. Yersin, A., H. Hirling, …, S. Kasas. 2003. Interactions between synaptic vesicle fusion proteins explored by atomic force microscopy. *Proc. Natl. Acad. Sci. USA.* 100:8736–8741.
17. Rickman, C., K. Hu, …, B. Davletov. 2005. Self-assembly of SNARE fusion proteins into star-shaped oligomers. *Biochem. J.* 388:75–79.
18. Karatekin, E., J. Di Giovanni, …, J. E. Rothman. 2010. A fast, single-vesicle fusion assay mimics physiological SNARE requirements. *Proc. Natl. Acad. Sci. USA.* 107:3517–3521.
19. Chang, C.-W., E. Hui, …, M. B. Jackson. 2015. A structural role for the synaptobrevin 2 transmembrane domain in dense-core vesicle fusion pores. *J. Neurosci.* 35:5772–5780.
20. Hernandez, J. M., A. J. Kreutzberger, …, R. Jahn. 2014. Variable cooperativity in SNARE-mediated membrane fusion. *Proc. Natl. Acad. Sci. USA.* 111:12037–12042.
21. Margittai, M., H. Otto, and R. Jahn. 1999. A stable interaction between syntaxin 1a and synaptobrevin 2 mediated by their transmembrane domains. *FEBS Lett.* 446:40–44.
22. Laage, R., J. Rohde, …, D. Langosch. 2000. A conserved membrane-spanning amino acid motif drives homomeric and supports heteromeric assembly of presynaptic SNARE proteins. *J. Biol. Chem.* 275:17481–17487.
23. Kroch, A. E., and K. G. Fleming. 2006. Alternate interfaces may mediate homomeric and heteromeric assembly in the transmembrane domains of SNARE proteins. *J. Mol. Biol.* 357:184–194.
24. Laage, R., and D. Langosch. 1997. Dimerization of the synaptic vesicle protein synaptobrevin (vesicle-associated membrane protein) II depends on specific residues within the transmembrane segment. *Eur. J. Biochem.* 249:540–546.
25. Hohl, T. M., F. Parlati, …, H. Engelhardt. 1998. Arrangement of subunits in 20 S particles consisting of NSF, SNAPs, and SNARE complexes. *Mol. Cell.* 2:539–548.
26. Mascia, L., and D. Langosch. 2007. Evidence that late-endosomal SNARE multimerization complex is promoted by transmembrane segments. *Biochim. Biophys. Acta.* 1768:457–466.
27. Bowen, M. E., D. M. Engelman, and A. T. Brunger. 2002. Mutational analysis of synaptobrevin transmembrane domain oligomerization. *Biochemistry.* 41:15861–15866.
28. Zhang, Y., and Y.-K. Shin. 2006. Transmembrane organization of yeast syntaxin-analogue Sso1p. *Biochemistry.* 45:4173–4181.
29. Fasshauer, D., W. K. Eliason, …, R. Jahn. 1998. Identification of a minimal core of the synaptic SNARE complex sufficient for reversible assembly and disassembly. *Biochemistry.* 37:10354–10362.
30. Bu, L., W. Im, and C. L. Brooks, 3rd. 2007. Membrane assembly of simple helix homo-oligomers studied via molecular dynamics simulations. *Biophys. J.* 92:854–863.
31. Nguyen, T. H. T., Z. Liu, and P. B. Moore. 2013. Molecular dynamics simulations of homo-oligomeric bundles embedded within a lipid bilayer. *Biophys. J.* 105:1569–1580.
32. Wassenaar, T. A., K. Pluhackova, …, R. A. Böckmann. 2015. High-throughput simulations of dimer and trimer assembly of membrane proteins. The DAFT approach. *J. Chem. Theory Comput.* 11:2278–2291.
33. Han, J., K. Pluhackova, …, R. A. Böckmann. 2015. Synaptobrevin transmembrane domain dimerization studied by multiscale molecular dynamics simulations. *Biophys. J.* 109:760–771.
34. Larisch, N., S. A. Kirsch, …, P. Dietrich. 2015. The function of the two-pore channel TPC1 depends on dimerization of its carboxy-terminal helix. *Cell. Mol. Life Sci.* Published online January 18, 2016. http://dx.doi.org/10.1007/s00018-016-2131-3.
35. Fleming, K. G., and D. M. Engelman. 2001. Computation and mutagenesis suggest a right-handed structure for the synaptobrevin transmembrane dimer. *Proteins* Struc. Func. *Bioinf.* 45:313–317.
36. Borisovska, M., Y. N. Schwarz, …, D. Bruns. 2012. Membrane-proximal tryptophans of synaptobrevin II stabilize priming of secretory vesicles. *J. Neurosci.* 32:15983–15997.
37. Langosch, D., J. M. Crane, …, J. Reed. 2001. Peptide mimics of SNARE transmembrane segments drive membrane fusion depending on their conformational plasticity. *J. Mol. Biol.* 311:709–721.
38. Hess, B., C. Kutzner, …, E. Lindahl. 2008. GROMACS 4: algorithms for highly efficient, load-balanced, and scalable molecular simulation. *J. Chem. Theory Comput.* 4:435–447.

39. Marrink, S. J., H. J. Risselada, …, A. H. de Vries. 2007. The MARTINI force field: coarse grained model for biomolecular simulations. *J. Phys. Chem. B.* 111:7812–7824.

40. Monticelli, L., S. K. Kandasamy, …, S.-J. Marrink. 2008. The MARTINI coarse-grained force field: extension to proteins. *J. Chem. Theory Comput.* 4:819–834.

41. Bussi, G., D. Donadio, and M. Parrinello. 2007. Canonical sampling through velocity rescaling. *J. Chem. Phys.* 126:014101.

42. Berendsen, H. J. C., J. P. M. Postma, …, J. R. Haak. 1984. Molecular dynamics with coupling to an external bath. *J. Chem. Phys.* 81:3684–3690.

43. Pluhackova, K., T. A. Wassenaar, and R. A. Böckmann. 2013. Molecular dynamics simulations of membrane proteins. *In* Membrane Biogenesis, *Vol. 1033*. D. Rapaport, and J. M. Herrmann, editors. Humana Press, New York, pp. 85–101.

44. Wassenaar, T. A., H. I. Ingólfsson, …, S. J. Marrink. 2015. Computational lipidomics with insane: a versatile tool for generating custom membranes for molecular simulations. *J. Chem. Theory Comput.* 11:2144–2155.

45. Wassenaar, T. A., K. Pluhackova, …, D. P. Tieleman. 2014. Going backward: a flexible geometric approach to reverse transformation from coarse grained to atomistic models. *J. Chem. Theory Comput.* 10:676–690.

46. Klauda, J. B., R. M. Venable, …, R. W. Pastor. 2010. Update of the CHARMM all-atom additive force field for lipids: validation on six lipid types. *J. Phys. Chem. B.* 114:7830–7843.

47. Best, R. B., X. Zhu, …, A. D. Mackerell, Jr. 2012. Optimization of the additive CHARMM all-atom protein force field targeting improved sampling of the backbone φ, ψ and side-chain $\chi(1)$ and $\chi(2)$ dihedral angles. *J. Chem. Theory Comput.* 8:3257–3273.

48. MacKerell, A. D., D. Bashford, …, M. Karplus. 1998. All-atom empirical potential for molecular modeling and dynamics studies of proteins. *J. Phys. Chem. B.* 102:3586–3616.

49. Darden, T., D. York, and L. Pedersen. 1993. Particle mesh Ewald: an N log(N) method for Ewald sums in large systems. *J. Chem. Phys.* 98:10089–10092.

50. Parrinello, M., and A. Rahman. 1981. Polymorphic transitions in single crystals: a new molecular dynamics method. *J. Appl. Phys.* 52:7182–7190.

51. Nosé, S. 1984. A molecular dynamics method for simulations in the canonical ensemble. *Mol. Phys.* 52:255–268.

52. Hoover, W. G. 1985. Canonical dynamics: equilibrium phase-space distributions. *Phys. Rev. A Gen. Phys.* 31:1695–1697.

53. Hess, B., H. Bekker, …, J. G. E. M. Fraaije. 1997. LINCS: a linear constraint solver for molecular simulations. *J. Comput. Chem.* 18:1463–1472.

54. Schrödinger, L. L. C. 2010. The PyMOL Molecular Graphics System, Version 1.3r1. http://www.schrodinger.com/.

55. Humphrey, W., A. Dalke, and K. Schulten. 1996. VMD: visual molecular dynamics. *J. Mol. Graph.* 14:33–38.

56. Lu, X., Y. Zhang, and Y.-K. Shin. 2008. Supramolecular SNARE assembly precedes hemifusion in SNARE-mediated membrane fusion. *Nat. Struct. Mol. Biol.* 15:700–706.

57. Fdez, E., M. Martínez-Salvador, …, S. Hilfiker. 2010. Transmembrane-domain determinants for SNARE-mediated membrane fusion. *J. Cell Sci.* 123:2473–2480.

58. Xu, Y., F. Zhang, …, Y.-K. Shin. 2005. Hemifusion in SNARE-mediated membrane fusion. *Nat. Struct. Mol. Biol.* 12:417–422.

59. Periole, X., T. Huber, …, T. P. Sakmar. 2007. G protein-coupled receptors self-assemble in dynamics simulations of model bilayers. *J. Am. Chem. Soc.* 129:10126–10132.

60. Blanchard, A. E., M. J. Arcario, …, E. Tajkhorshid. 2014. A highly tilted membrane configuration for the prefusion state of synaptobrevin. *Biophys. J.* 107:2112–2121.

61. Han, J., K. Pluhackova, D. Bruns, and R. A. Böckmann. 2016. Synaptobrevin transmembrane domain determines the structure and dynamics of the SNARE motif and the linker region. *Biochim. Biophys. Acta.* 1858:855–865.

62. Shi, L., Q.-T. Shen, …, F. Pincet. 2012. SNARE proteins: one to fuse and three to keep the nascent fusion pore open. *Science.* 335:1355–1359.

63. Domanska, M. K., V. Kiessling, …, L. K. Tamm. 2009. Single vesicle millisecond fusion kinetics reveals number of SNARE complexes optimal for fast SNARE-mediated membrane fusion. *J. Biol. Chem.* 284:32158–32166.

64. Bar-On, D., S. Wolter, …, U. Ashery. 2012. Super-resolution imaging reveals the internal architecture of nano-sized syntaxin clusters. *J. Biol. Chem.* 287:27158–27167.

65. Sieber, J. J., K. I. Willig, …, T. Lang. 2007. Anatomy and dynamics of a supramolecular membrane protein cluster. *Science.* 317:1072–1076.

66. Takamori, S., M. Holt, …, R. Jahn. 2006. Molecular anatomy of a trafficking organelle. *Cell.* 127:831–846.